PHYSICAL REVIEW B **107**, 115167 (2023)

Nonsymmorphic symmetry protected spin-orbit semi-Dirac fermions in two dimensions

Weizhen Meng, Ying Liu,[*] Xiaoming Zhang, Zeqing He, Wei-Wang Yu, Huai Zhang,
Lu Tian, and Guodong Liu[†]

State Key Laboratory of Reliability and Intelligence of Electrical Equipment, Hebei University of Technology, Tianjin 300130, China
and School of Materials Science and Engineering, Hebei University of Technology, Tianjin 300130, China

(Received 19 October 2022; revised 1 March 2023; accepted 16 March 2023; published 30 March 2023)

Semi-Dirac fermions (SDFs) in two-dimensional (2D) systems, which simultaneously exhibit linear and quadratic dispersion around them, are a bridge linking linear and quadratic Dirac cones. However, the so-called SDFs in the reported 2D materials are doubly degenerate (namely semi-Weyl fermions), and are vulnerable against spin-orbital coupling (SOC). Here, we propose a 2D SOC-robust SDF which arises from nonsymmorphic symmetries. Unlike the known 2D SDFs, due to the presence of inversion and time reversal symmetries ($\mathcal{IT}$), each crossing band is doubly degenerate, making the SDF of fourfold degeneracy. By high throughput screening, we find that 26 candidate 2D materials (such as $CuCN_2$, CaI_2, TlF) can hold SDFs, which belong to layer groups 40 (*pmam*), 43 (*pbaa*), and 45 (*pbma*), respectively. Furthermore, the symmetry protection mechanism, associated Fermi arc edge states, the catalytic performance, and the topological phase transitions under symmetry breaking of SDFs are revealed, providing a way for understanding 2D SOC-robust SDFs. Overall, our work proposes a class of topological phases, and provides a platform to study their fascinating physical effects.

DOI: 10.1103/PhysRevB.107.115167

I. INTRODUCTION

The advent of topological semimetals (TSMs) has drawn wide attention in the past decades [1,2], of which graphene [3] is a prominent example. The conduction and valence bands in monolayer graphene linearly touch at the K/K' valley of momentum space. Among them, the electrons around the linear crossing point can effectively emulate Dirac fermions in two dimensions (2D) [4–6]. Thus, many fascinating physical effects of monolayer graphene come from the linear 2D Dirac point, such as high Fermi speed [7], conical diffraction [8], etc. In addition, the 2D Dirac cone in graphene is isotropic in the low-energy region, giving rise to massless properties along all directions. It is prudent to mention that the isotropic Dirac cone can be tuned by an external field, e.g., the magnetic field [9] and a uniaxial strain [10], giving rise to the so-called semi-Dirac fermion (SDF). The SDF only resembles the massless 2D Dirac point in one direction, but it behaves as a zero-gap semiconductor in the perpendicular direction, with an effective mass feature. Such a feature leads to unique properties of the transport properties [11] and light absorption [12] for semi-Dirac semimetals/metals. So far, several 2D materials or classical systems have been predicted to host such a SDF, such as black phosphorous [13], magnetic heterostructure TiO_2/VO_2 [14,15], and photonic crystals [16].

However, the previously reported 2D SDFs were not comprehensive. First, the so-called SDF is a twofold crossing point rather than a fourfold degenerate one. In fact, it is a semi-Weyl fermion (SWF). Second, the presence of 2D SWFs requires the imposition of additional interference terms, such as the external fields or constructing a heterojunction [10,14,15]. Third, the SWFs are broken when considering spin-orbital coupling (SOC), leading to the quantum spin Hall effect. Then the question naturally arises: Is it possible to have a spin-orbit 2D realistic SDF with a fourfold degeneracy? If so, which symmetry protects it? And what are its characteristic?

Young and Kane [17] have verified that a 2D Dirac point with fourfold degeneracy can exist under SOC. The Dirac point consists of two Weyl points with opposite chirality ($\chi = \pm 1$) and is protected by nonsymmorphic symmetries, as shown in Fig. 1(a). Subsequently, a large number of 2D materials with Dirac points have been predicted, such as the monolayer HfGeTe family [18], monolayer X_3SiTe_6 ($X =$ Ta, Nb) [19], monolayer SbSSn [20], also including several antiferromagnetic materials, such as monolayer FeSe [21], monolayer XFe_2As_2 ($X =$ Ba, Sr) [22], monolayer Zr_2Si [23], and 2D $TaCoTe_2$ [24]. However, these Dirac fermions exhibit linear dispersion along all directions, as shown in Fig. 1(b)(i). Therefore, it is urgent to find SOC-robust SDFs in 2D systems. That is, one direction shows a linear dispersion and the other presents a quadratic dispersion [see Fig. 1(b)(ii)].

In this paper, we address the questions raised before. We find that the topological phases with SDFs can exist in 2D spinful systems. The stability of the SDFs is protected by nonsymmorphic symmetries and time-reversal symmetry ($\mathcal{T}$). In our previous work [25], we have found that 65 candidate two-dimensional materials possess a SOC-robust Dirac point. After further screening, we find 26 2D candidate materials capable of hosting SDFs (see Table I). Among them, our key findings are as follows: (i) The low-energy electrons around these SDFs behave as massless particles in one spatial

---

[*] ying_liu@hebut.edu.cn

[†] gdliu1978@126.com

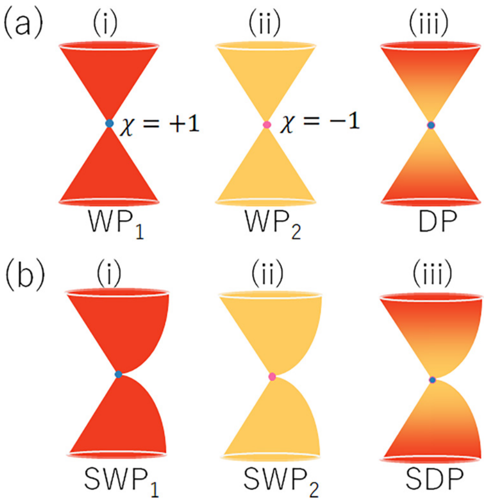

FIG. 1. (a) Three-dimensional dispersion bands of two linear Weyl points with opposite chirality [(i) and (ii)] and a linear Dirac point (iii). (b) The three-dimensional dispersion bands of two semi-Weyl points with opposite chirality [(i) and (ii)] and a semi-Dirac point (iii).

direction and as massive ones in the other directions. (ii) All the SDFs are located at the time-reversal invariant momentum (TRIM), which indicates $\mathcal{T}$ plays an important role in the presence of SDFs. (iii) The electron and hole pockets surrounding the SDF exhibit an elliptical shape, resulting in a helical Fermi surface. Then, these results are further demonstrated by a symmetry analysis and phase transitions. Based on the candidate materials, we further show that the SDFs are characterized by distinct edge states, which are different from the linear Dirac points. Taking the monolayer CuCN$_2$ as a candidate material, we systematically verify these results. Furthermore, a 3D counterpart of monolayer CuCN$_2$ was synthesized in the experiment [26,27]. Remarkably, the phonon spectrum and thermodynamic stability have proved that the monolayer CuCN$_2$ is stable at room temperature. SDFs only exhibit their edge states along the direction with a quadratic dispersion, while the linear dispersion direction does not have edge states. [See Fig. 1(b)(iii)]. Overall, our work provides a platform to study the SDFs in 2D systems.

II. CALCULATION METHODS

The numerical calculations in the current work were performed within the Vienna *ab initio* simulation package (VASP) [28] in the framework of density-functional theory (DFT) [29]. The generalized gradient approximation (GGA) of the Perdew-Burke-Ernzerhof (PBE) method [30] was applied for the exchange-correlation potential. The cutoff energy was adopted as 500 eV, and the Brillouin zone (BZ) was sampled with a Γ-centered k-point mesh of 15 × 15 × 1. The DFT-D2 method [31] was used to consider the long-range van der Waals interactions. A vacuum layer of 20 Å thickness is added to avoid artificial interactions between periodic images. The PHONOPY code [32] was used to calculate the phonon spectra, with a 6 × 6 × 1 supercell and a 4 × 4 × 1 q grid. The edge states are calculated by using Wannier functions [33,34] and the iterative Green's function method [35] as implemented in the WANNIERTOOLS package [36].

III. RESULTS

A. SDFs in monolayer CuCN$_2$

We find that screened 26 actual materials belong to layer groups (LG) 40 (*pmam*), 43 (*pbaa*), and 45 (*pbma*), respectively (see Supplemental Material [37]). According to the screened candidate materials (including the CuCN$_2$) [37], we find that all the crystal structures have a nonequilateral honeycomb hexagonal lattice, which are similar to the regular hexagonal lattice with uniaxial strain. Next, taking monolayer CuCN$_2$ of LG 40 as an example, we systematically study the properties of the SDFs by DFT calculations and theoretical analysis.

As shown in Fig. 2(a), the crystal structure of monolayer CuCN$_2$ belongs to LG 40, which can be generated by the following generations: two rotation symmetries, namely $\widetilde{\mathcal{C}}_{2z} : (x, y, z) \rightarrow (-x + 1/2, -y, z)$, $\mathcal{C}_{2y} : (x, y, z) \rightarrow (-x, y, -z)$, the inversion symmetry ($\mathcal{I}$). Here, the tilde (∼) refers to a half translation. In addition, no magnetic ordering is found in this material, thus, the time-reversal symmetry ($\mathcal{T}$) is preserved. For monolayer CuCN$_2$, its lattice parameters ($a = 2.96$ Å, $b = 9.41$ Å) and the bond lengths of C-N ($d = 1.23$ Å) and Cu-N ($d = 1.99$ Å) are shown in Fig. 2(a). Figure 2(b) shows the electron localized function (ELF) of monolayer CuCN$_2$. We find that C and N atoms form a strong covalent bond, while Cu and N atoms form an ionic bond. From the projected density of states (PDOS) [see Fig. 3(a)], the ionic bond plays a dominant role in the band near the Fermi level. In addition, we calculate its phonon spectrum, as shown in Fig. 2(c), finding that there are no virtual frequencies along all k paths (Γ-Y-S-Γ), meaning that monolayer CuCN$_2$ is dynamically stable. Then, we investigate its electronic band structure via the first-principles calculations.

We plot the electronic band structure and the PDOS of the monolayer CuCN$_2$ in Fig. 3(a). From the PDOS, one can observe that this material shows a metal feature, and the bands in the low-energy region are mainly contributed by the 3d orbital of the Cu atom and the 2p orbital of the N atom. In

TABLE I. SDFs in 2D systems. We list the possible layer groups (LGs) with considering the SOC. PGs stands for point groups, and candidate materials.

LGs	Positions	PGs	Operators	Candidate materials
40	X, S	D_{2h}	$\{\widetilde{\mathcal{C}}_{2z}\vert\frac{1}{2}00\}, \mathcal{C}_{2y}, \mathcal{I}, \mathcal{T}$	CuCN$_2$, LiCuO, Ag/Cu$_2$Te/Se, Ag/CuF/Br/Cl/I, Na$_2$Cl, CaI$_2$
43	Y		$\{\widetilde{\mathcal{C}}_{2x}\vert 0\frac{1}{2}0\}, \{\widetilde{\mathcal{C}}_{2z}\vert\frac{1}{2}00\}, \mathcal{I}, \mathcal{T}$	Ru/FeSe/S$_2$, AgClO$_2$
45	X, S		$\{\widetilde{\mathcal{C}}_{2y}\vert 0\frac{1}{2}0\}, \{\widetilde{\mathcal{C}}_{2x}\vert\frac{1}{2}\frac{1}{2}0\}, \mathcal{I}, \mathcal{T}$	TlF, BF/Cl/Br/I

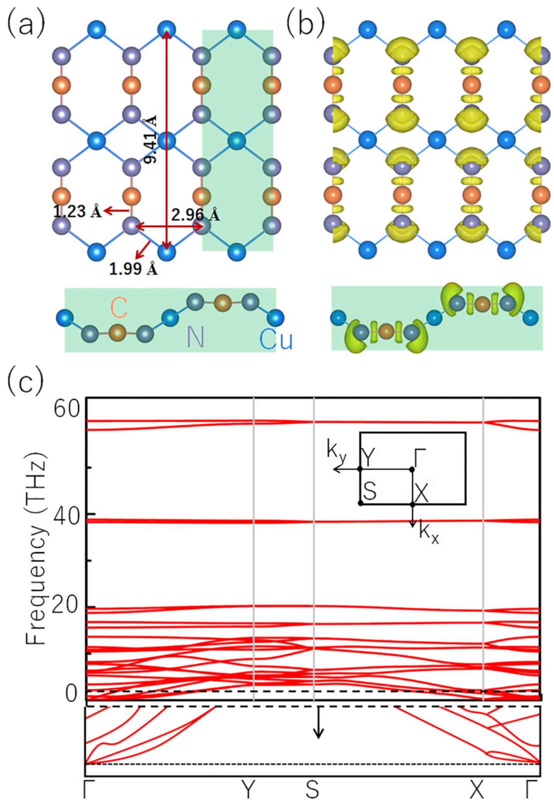

FIG. 2. (a) Top and side views of the crystal structure of the monolayer $\mathrm{CuCN_2}$, where the green shaded part indicates the primitive cell. (b) The electron localized function (ELF) of $\mathrm{CuCN_2}$, with isosurface 0.8, (c) Phonon spectrum of the monolayer $\mathrm{CuCN_2}$. The inset is the Brillouin zone of its monolayer.

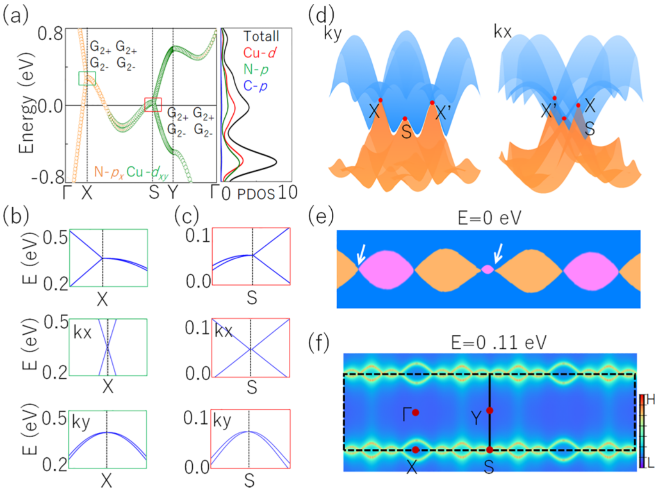

FIG. 3. (a) Band structure of the monolayer $\mathrm{CuCN_2}$ with SOC. The right panel shows its PDOS. (b) and (c) Zoom-in band structures, indicating the SDFs at the X and S points. (d) The 3D bands near points X and S along the k_x and k_y directions. (e) Morphology of carriers for two SDFs at point S, where the white arrow shows where the electron and hole pockets meet. (f) Morphology of Fermi surface at $E = 0.11$ eV.

addition, it is worth noting that each band in its electronic band structure is of double degeneracy due to $(\mathcal{I}\mathcal{T})^2 = -1$ when including SOC. Moreover, the inversion symmetry and $\widetilde{C}_{2z}$ symmetry satisfy $\mathcal{I}\widetilde{C}_{2z} = e^{-ik_x}\widetilde{C}_{2z}\mathcal{I}$. Thus, there exists $\{\mathcal{I}, \widetilde{C}_{2z}\}$ at the X, S points. Consequently, the crossing points at the X and S points are fourfold degenerated, called the 2D Dirac point. In addition, the irreducible representations (IRs) (namely $\Gamma_{2+} + \Gamma_{2+} + \Gamma_{2-} + \Gamma_{2-}$) at the X and S points also verify the existence of Dirac points.

Most interestingly, we can find that the crossing points at X and S exhibit a linear dispersion along the k_x direction, whereas a quadratic dispersion is shown along the k_y direction, as shown in the enlarged views in Figs. 3(b) and 3(c). The effective Hamiltonian for the Dirac points at the X/S points have been constructed in the Supplemental Material [37]. By fitting the real parameters in the Hamiltonian, one can see that the dispersion in the k_y direction is quadratic, while the dispersion in the k_x direction is linear. Then, we denote the Dirac points at the X, S points as the 2D SDFs. Also, we plot the 3D dispersion bands near points X and S, as shown in Fig. 3(d). More intuitively, linear and quadratic dispersions along the k_x and k_y directions are observed. Notably, due to the anisotropic band structures, the electronic pocket (EP) and hole pocket (HP) of monolayer $\mathrm{CuCN_2}$ exhibit elliptical shapes in momentum space, as shown in Fig. 3(e). Moreover, the SDFs at points X and S are linked by a HP and EP with approximate ellipse morphology. Remarkably, if we give a energy slice at -0.4 to 0.4 eV, e.g., $E = 0.11$ eV, the Fermi surfaces along the k path S-X show the spiral morphology [see Fig. 3(f)]. The above results indicate that the SDF supports highly anisotropic behaviors in momentum space, which may bring unique transport properties. For example, due to the coexistence of massless and massive Dirac fermions, it is expected to show a distinct Landau-level spectrum under a magnetic field [9,38].

B. Edge states and catalytic performance

A nontrivial topological phase can be diagnosed by the presence of edge states. For example, a 2D topological insulator is characterized by the helical edge states inside the gap, as shown in Fig. 4(a)(i). In sharp contrast, two 2D Weyl fermions with opposite chirality are connected by a Fermi arc, as indicated in Fig. 4(a)(ii). Certain symmetries can enforce the two Weyl points with opposite chirality stabilize at the same position, forming a Dirac point. If these symmetries contain the $\mathcal{I}\mathcal{T}$ symmetries, there is no edge state stemming from the projection of Dirac points due to the disappearance of the Berry curvature, as demonstrated in Fig. 4(a)(iii). In comparison, the edge states will appear when breaking $\mathcal{I}$ symmetry. In addition, it has been well studied that there exist edge states stemming from the quadratic Dirac point located at the time-reversal invariant momentum [see Fig. 4(a)(iv)] [39,40]. One may consider the following: How are the edge states associated with the distribution of 2D SDFs?

To address this question, we plot the edge states for the monolayer $\mathrm{CuCN_2}$, as shown in Figs. 4(b) and 4(d). We can clearly find that there are no edge states along linear dispersion direction (namely the k_x direction). However, there exist two Fermi arc edge states emanating from the projection of

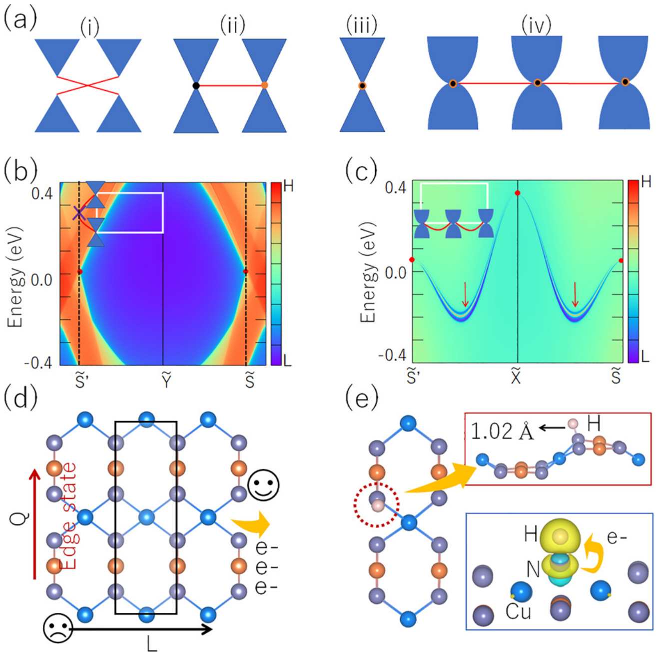

FIG. 4. The classification of 2D topological phases. The black and yellow dots indicate the crossing point of opposite chirality. The red lines represent the edge states. (a) (i) The edge states of 2D topological insulators (TIs) with SOC. (ii) A Fermi arc links a pair of 2D Weyl points of opposite chirality. (iii) Linear 2D Dirac points with the presence of spacetime inversion ($\mathcal{IT}$) symmetry. (iv) Two Fermi arcs link a pair of quadratic Dirac points in a 2D system. (b) and (c) The edge states of monolayer $CuCN_2$ along the linear and quadratic directions, where the insets are schematic diagrams of the edge states. (d) Diagram of hydrogen evolution reaction for monolayer $CuCN_2$, where "Q" and "L" represent the quadratic and linear dispersions, respectively. (e) Top view and side view of optimized $CuCN_2H$, where 1.02 Å is the bond length of N-H. Differential charge density (DCD) of hydrogen adsorbed by $CuCN_2$, where blue and yellow represent electrons losing and electrons gaining, respectively.

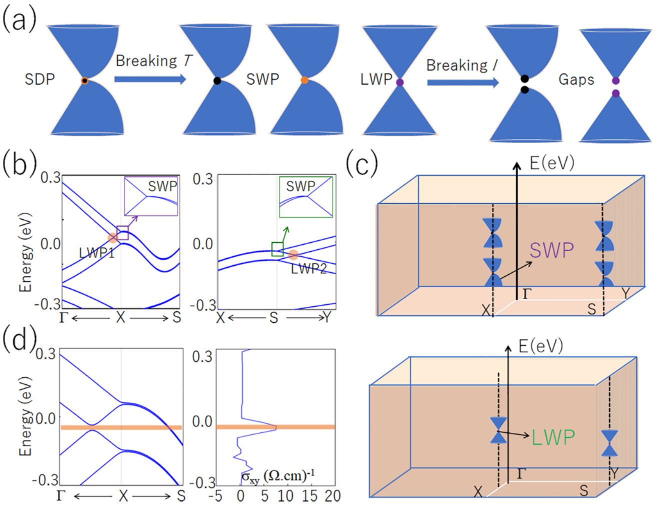

FIG. 5. (a) Schematic diagram for the topological phase transitions under symmetry breaking: (i) A SDP is transformed into a pair of semi-Weyl fermions (SWFs) under breaking $\mathcal{T}$. (ii) Further breaking inversion symmetry, the SWFs are broken. (b) shows the electronic band structures when breaking $\mathcal{T}$ symmetry by applying a magnetic field normal to monolayer $CuCN_2$. The insets are the enlarged views for the SWFs points at the X, S points. (c) The schematic figure for the positions of SWPs and LWPs in BZ. (d) A gap is introduced at SWFs when breaking the $\mathcal{I}$ symmetry, along with its anomalous Hall conductivity.

SDFs along the quadratic dispersion direction (namely the k_y direction). Remarkably, based on the previous reports of Young *et al.* [17] and Jin *et al.* [20], 2D linear Dirac points do not have the Fermi arc edge states in inversion and time reversal symmetries, which are different from 2D SOC SDPs.

Remarkably, topological catalysis is a hot topic in current research [41–43]. It is well known that high carrier mobility, high electronic densities near the Fermi level, and low Gibbs free energy (ΔG) are three crucial parameters to determine the catalytic activity in catalysts [41,42,44–46]. We find that all of them are significantly affected by the Dirac points and Fermi arcs of $CuCN_2$. First, benefiting from the band crossings and the Fermi arc edge/surface states, 2D/3D topological semimetals commonly possess high carrier mobility, which have also been demonstrated experimentally [44,47,48]. For monolayer $CuCN_2$, Fermi arc boundary states exist only in the quadratic dispersion direction (namely the k_y direction). Therefore, $CuCN_2$ can provide a good adsorption effect along the k_y direction, as shown in Fig. 4(d). Second, the Fermi arc edge states in $CuCN_2$ can induce high electronic density of states on the boundary which then improve the catalytic performance. The electronic density at the Fermi level for the quadratic direction is two times (8.02 electrons/eV vs 3.97 electrons/eV) larger than that of the linear dispersion direction. A similar phenomenon was also found in some other topological materials, such as Weyl semimetal NiSi [49], multifold nodal points $12CaO{\cdot}7Al_2O_3$ (C12A7:$4e^-$) [46], multiple fermions Ba_4Al_5 [50], etc. Then, based on DFT calculation, we find that the boundary N atoms of the k_y direction are the most stable adsorption site in $CuCN_2$ for a hydrogen evolution reaction (HER), and the adsorption energy is about−0.33 eV, as shown in Fig. 4(e) (adsorption energy expression: $E_{\mathrm{ads}} = E_{\mathrm{CuCN_2+H}} - E_{\mathrm{CuCN_2}} - 1/2E_{\mathrm{H_2}}$). From the differential charge density (DCD), it is obvious that the p-orbital electrons of N atoms are transferred to the H atom. Finally, the Gibbs free energy (ΔG) is calculated as −0.11 eV, indicating that $CuCN_2$ has a high catalytic performance in HER (the expression of Gibbs free energy $\Delta G = E_{\mathrm{ads}} + \Delta E_{\mathrm{ZPE}} - T\Delta S_{\mathrm{H}}$, where ΔE_{ZPE} is the change of the zero-point energy, and $T\Delta S_{\mathrm{H}}$ is the entropy). Therefore, we provide a good platform for understanding topological catalysis.

C. Phase transitions

Since the SDFs are protected by nonsymmorphic symmetries, it is interesting to study the phase transition under symmetry breaking. Similar to the conventional Dirac points, a 2D SDF is expected to be transformed into a pair of 2D semi-Weyl fermions (SWFs) with opposite chirality when breaking $\mathcal{T}$ symmetry. Further breaking the $\mathcal{I}$ symmetry, the 2D SWFs are broken, as shown in Fig. 5(a). Based on the realistic material $CuCN_2$, we destroy the $\mathcal{T}$ symmetry via applying a magnetic field normal to the material. As shown in

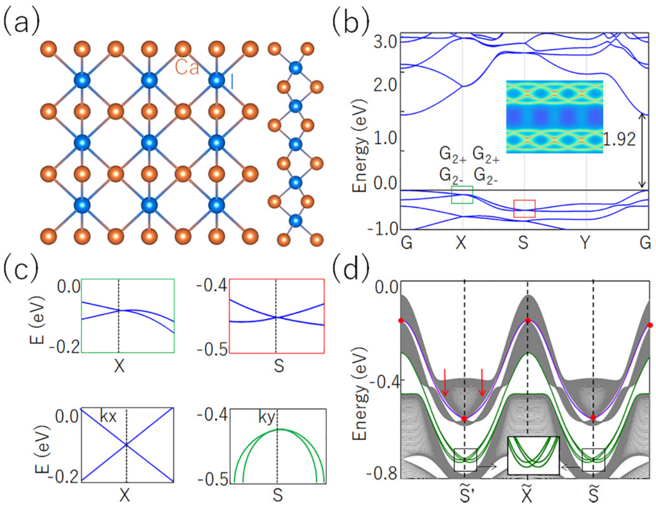

FIG. 6. (a) The crystal structure for monolayer CaI_2. (b) The electronic band structure of monolayer CaI_2, where the inset is the Fermi surface at the Fermi level. (c) Local enlargements of the bands of the green and red boxes in (b), as well as band structures near points X and S along the k_x and k_y directions, respectively. (d) The edge states of monolayer CaI_2 along the quadratic dispersion direction, where the red dots and arrows indicate the positions of the SDFs and the Fermi arc edge states, respectively. The green shows that there are hourglass edge states between the band gaps of the two SDFs.

Fig. 5(b), the SDF at the X or S point transforms into a pair of SWFs at different energies, as shown in Fig. 5(b). In addition, a pair of linear Weyl points (LWPs) appear along Γ-X/S-Y due to the band splitting. The positions of SWFs and LWPs in BZ are schematically given in Fig. 5(c). In the following, we also study the results with further breaking the $\mathcal{I}$ symmetry. By shifting the center Cu atom, the $\mathcal{I}$ symmetry is destroyed, then both SWFs and LWFs open a tiny gap [see the left panel in Fig. 5(d)]. Particularly, the band gap of LWFs is larger than one of the SWFs, thus generating an intrinsically anomalous Hall conductance at the band gap of the LWFs (about 7.58 $\Omega\,\mathrm{cm}^{-1}$), as shown in the right panel in Fig. 5(d). Therefore, when a series of additional perturbations are applied to semi-Dirac semimetal/metals, SDFs exhibit rich topological phase transitions.

IV. DISCUSSION AND CONCLUSION

We also identify a semiconductor with SDFs in LG 40, namely monolayer CaI_2. The band gap of monolayer CaI_2 is 1.92 eV, and SDFs are found at points X and S [see Figs. 6(a)–6(c)]. Similar to $CuCN_2$, two Fermi arc edge states also originate from the Dirac cone with a quadratic dispersion direction. Interestingly, we also observe hourglass edge states in the energy gap below SDFs, which are protected by nonsymmorphic symmetries, as shown in Fig. 6(d). In addition, these materials with SDFs belonging to LGs 40, 43, and 45 are also studied in our work. We provide the crystal structures, electronic band structures, and the theoretical analysis in the Supplemental Material (see Table SI and Figs. S1– S4) [37].

In conclusion, we reveal a topological phase (namely SDF) that manifests unique features in 2D electronic systems, including the highly anisotropic dispersion, unique edge states, excellent catalytic performance, and interesting phase transitions. This work provides a platform to understand the 2D Dirac point. Then, taking $CuCN_2$ as an example, we verify the presence of SDFs by DFT calculations and theory analysis. Monolayer $CuCN_2$ has a clean band structure, without any other band crossings around the SDFs. Thus, in experiments, its energy dispersion may be clearly seen by the angle-resolved photoemission spectroscopy (ARPES).

ACKNOWLEDGMENTS

This work is supported by National Natural Science Foundation of China (Grant No. 12004096), “100 Talents Plan” of Hebei Province (No. E2020050014). One of the authors (X.M.Z.) acknowledges the financial support from Young Elite Scientists Sponsorship Program by Tianjin. Postgraduate Innovation Funding Project of Hebei Province (No.CXZZBS2022036)

---

[1] N. P. Armitage, E. J. Mele, and A. Vishwanath, Weyl and Dirac semimetals in three-dimensional solids, Rev. Mod. Phys. **90**, 015001 (2018).

[2] B. Q. Lv, T. Qian, and H. Ding, Experimental perspective on three-dimensional topological semimetals, Rev. Mod. Phys. **93**, 025002 (2021).

[3] K. S. Novoselov, A. K. Geim, S. V. Morozov, D.-e. Jiang, Y. Zhang, S. V. Dubonos, I. V. Grigorieva, and A. A. Firsov, Electric field effect in atomically thin carbon films, Science **306**, 666 (2004).

[4] A. H. Castro Neto, F. Guinea, N. M. R. Peres, K. S. Novoselov, and A. K. Geim, The electronic properties of graphene, Rev. Mod. Phys. **81**, 109 (2009).

[5] A. K. Geim, Graphene: Status and prospects, Science **324**, 1530 (2009).

[6] A. K. Geim and K. S. Novoselov, The rise of graphene, Nat. Mater. **6**, 183 (2007).

[7] K. S. Novoselov, A. K. Geim, S. V. Morozov, D. Jiang, M. I. Katsnelson, I. Grigorieva, S. Dubonos, and A. A. Firsov, Two-dimensional gas of massless Dirac fermions in graphene, Nature (London) **438**, 197 (2005).

[8] O. Peleg, G. Bartal, B. Freedman, O. Manela, M. Segev, and D. N. Christodoulides, Conical Diffraction and Gap Solitons in Honeycomb Photonic Lattices, Phys. Rev. Lett. **98**, 103901 (2007).

[9] P. Dietl, F. Piéchon, and G. Montambaux, New Magnetic Field Dependence of Landau Levels in a Graphenelike Structure, Phys. Rev. Lett. **100**, 236405 (2008).

[10] C. Zhong, Y. Chen, Y. Xie, Y.-Y. Sun, and S. Zhang, Semi-Dirac semimetal in silicene oxide, Phys. Chem. Chem. Phys. **19**, 3820 (2017).

[11] B. Real, O. Jamadi, M. Milićević, N. Pernet, P. St-Jean, T. Ozawa, G. Montambaux, I. Sagnes, A. Lemaître, L. Le Gratiet, A. Harouri, S. Ravets, J. Bloch, and A. Amo, Semi-Dirac Transport and Anisotropic Localization in Polariton Honeycomb Lattices, Phys. Rev. Lett. **125**, 186601 (2020).

[12] X. Zhou, W. Chen, and X. Zhu, Anisotropic magneto-optical absorption and linear dichroism in two-dimensional semi-Dirac electron systems, Phys. Rev. B **104**, 235403 (2021).

[13] J. Kim, S. S. Baik, S. H. Ryu, Y. Sohn, S. Park, B.-G. Park, J. Denlinger, Y. Yi, H. J. Choi, and K. S. Kim, Observation of tunable band gap and anisotropic Dirac semimetal state in black phosphorus, Science **349**, 723 (2015).

[14] V. Pardo and W. E. Pickett, Half-Metallic Semi-Dirac-Point Generated by Quantum Confinement in TiO_2/VO_2 Nanostructures, Phys. Rev. Lett. **102**, 166803 (2009).

[15] S. Banerjee, R. R. P. Singh, V. Pardo, and W. E. Pickett, Tight-Binding Modeling and Low-Energy Behavior of the Semi-Dirac Point, Phys. Rev. Lett. **103**, 016402 (2009).

[16] Y. Wu, A semi-Dirac point and an electromagnetic topological transition in a dielectric photonic crystal, Opt. Express **22**, 1906 (2014).

[17] S. M. Young and C. L. Kane, Dirac Semimetals in Two Dimensions, Phys. Rev. Lett. **115**, 126803 (2015).

[18] S. Guan, Y. Liu, Z.-M. Yu, S.-S. Wang, Y. Yao, and S. A. Yang, Two-dimensional spin-orbit Dirac point in monolayer HfGeTe, Phys. Rev. Mater. **1**, 054003 (2017).

[19] S. Li, Y. Liu, S.-S. Wang, Z.-M. Yu, S. Guan, X.-L. Sheng, Y. Yao, and S. A. Yang, Nonsymmorphic-symmetry-protected hourglass Dirac loop, nodal line, and Dirac point in bulk and monolayer X_3SiTe_6 (X = Ta, Nb), Phys. Rev. B **97**, 045131 (2018).

[20] Y. J. Jin, B. B. Zheng, X. L. Xiao, Z. J. Chen, Y. Xu, and H. Xu, Two-Dimensional Dirac Semimetals without Inversion Symmetry, Phys. Rev. Lett. **125**, 116402 (2020).

[21] S. M. Young and B. J. Wieder, Filling-Enforced Magnetic Dirac Semimetals in Two Dimensions, Phys. Rev. Lett. **118**, 186401 (2017).

[22] Z.-G. Chen, L. Wang, Y. Song, X. Lu, H. Luo, C. Zhang, P. Dai, Z. Yin, K. Haule, G. Kotliar *et al.*, Two-Dimensional Massless Dirac Fermions in Antiferromagnetic AFe_2As_2 (A = Ba, Sr), Phys. Rev. Lett. **119**, 096401 (2017).

[23] X. Shao, X. Liu, X. Zhang, J. Wang, and M. Zhao, Zr_2Si: An antiferromagnetic Dirac MXene, Phys. Chem. Chem. Phys. **20**, 3946 (2018).

[24] S. Li, Y. Liu, Z.-M. Yu, Y. Jiao, S. Guan, X.-L. Sheng, Y. Yao, and S. A. Yang, Two-dimensional antiferromagnetic Dirac fermions in monolayer $TaCoTe_2$, Phys. Rev. B **100**, 205102 (2019).

[25] W. Meng, Y. Liu, W.-W. Yu, X. Zhang, and G. Liu, Spin-orbital robust Dirac points in two-dimensional systems, Mater. Today Phys. **27**, 100774 (2022).

[26] P. Jacobs, A. Houben, W. Schweika, A. L. Tchougréeff, and R. Dronskowski, Instrumental resolution as a function of scattering angle and wavelength as exemplified for the POWGEN instrument, J. Appl. Crystallogr. **50**, 866 (2017).

[27] Q. Liu, Y. Liu, G. Dai, L. Tian, J. Xu, G. Zhao, N. Zhang, and Y. Fang, Size-controllable synthesis of hierarchical copper carbodiimide microcrystals and their pronounced photoelectric response under visible light, Appl. Surf. Sci. **357**, 745 (2015).

[28] G. Kresse and D. Joubert, From ultrasoft pseudopotentials to the projector augmented-wave method, Phys. Rev. B **59**, 1758 (1999).

[29] J. J. Mortensen, L. B. Hansen, and K. W. Jacobsen, Real-space grid implementation of the projector augmented wave method, Phys. Rev. B **71**, 035109 (2005).

[30] V. I. Anisimov, J. Zaanen, and O. K. Andersen, Band theory and Mott insulators: Hubbard U instead of Stoner I, Phys. Rev. B **44**, 943 (1991).

[31] S. Grimme, Semiempirical GGA-type density functional constructed with a long-range dispersion correction, J. Comput. Chem. **27**, 1787 (2006).

[32] A. Togo, F. Oba, and I. Tanaka, First-principles calculations of the ferroelastic transition between rutile-type and $CaCl_2$-type SiO_2 at high pressures, Phys. Rev. B **78**, 134106 (2008).

[33] N. Marzari and D. Vanderbilt, Maximally localized generalized Wannier functions for composite energy bands, Phys. Rev. B **56**, 12847 (1997).

[34] I. Souza, N. Marzari, and D. Vanderbilt, Maximally localized Wannier functions for entangled energy bands, Phys. Rev. B **65**, 035109 (2001).

[35] A. A. Soluyanov and D. Vanderbilt, Computing topological invariants without inversion symmetry, Phys. Rev. B **83**, 235401 (2011).

[36] Q. Wu, S. Zhang, H.-F. Song, M. Troyer, and A. A. Soluyanov, WannierTools: An open-source software package for novel topological materials, Comput. Phys. Commun. **224**, 405 (2018).

[37] See Supplemental Material at http://link.aps.org/supplemental/10.1103/PhysRevB.107.115167 for a symmetry analysis, candidate materials, cell structure and electronic band structure of the candidate materials, and a two-dimensional database.

[38] P. Delplace and G. Montambaux, Semi-Dirac point in the Hofstadter spectrum, Phys. Rev. B **82**, 035438 (2010).

[39] W. Wu, Z. M. Yu, X. Zhou, Y. X. Zhao, and S. A. Yang, Higher-order Dirac fermions in three dimensions, Phys. Rev. B **101**, 205134 (2020).

[40] L. Tian, Y. Liu, W. Meng, X. Zhang, X. Dai, and G. Liu, Spin-orbit coupling-determined topological phase: Topological insulator and quadratic dirac semimetals, J. Phys. Chem. Lett. **11**, 10340 (2020).

[41] G. Li and C. Felser, Heterogeneous catalysis at the surface of topological materials, Appl. Phys. Lett. **116**, 070501 (2020).

[42] A. Politano, G. Chiarello, Z. Li, V. Fabio, L. Wang, L. Guo, X. Chen, and D. W. Boukhvalov, Toward the effective exploitation of topological phases of matter in catalysis: Chemical reactions at the surfaces of NbAs and TaAs Weyl semimetals, Adv. Funct. Mater. **28**, 1800511 (2018).

[43] X. Zhang, W. Meng, Y. Liu, X. Dai, G. Liu, and L. Kou, Magnetic electrides: High-throughput material screening, intriguing properties, and applications, J. Am. Chem. Soc. **145**, 5523 (2023).

[44] H. Luo, P. Yu, G. Li, and K. Yan, Topological quantum materials for energy conversion and storage, Nat. Rev. Phys. **4**, 611 (2022).

[45] G. Li, C. Fu, W. Shi, L. Jiao, J. Wu, Q. Yang, R. Saha, M. E. Kamminga, A. K. Srivastava, E. Liu *et al.*, Dirac nodal arc semimetal $PtSn_4$: An ideal platform for understanding surface properties and catalysis for hydrogen evolution, Angew. Chem. **131**, 13241 (2019).

[46] W. Meng, X. Zhang, Y. Liu, X. Dai, G. Liu, Y. Gu, E. Kenny, and L. Kou, Multifold fermions and Fermi arcs boosted catalysis in nanoporous electride $12CaO \cdot 7Al_2O_3$, Adv. Sci. **10**, 2205940 (2023).

[47] Y. Bai, F. Fei, S. Wang, N. Li, X. Li, F. Song, R. Li, Z. Xu, and P. Liu, High-harmonic generation from topological surface states, Nat. Phys. **17**, 311 (2021).

[48] M. Neupane, S.-Y. Xu, R. Sankar, N. Alidoust, G. Bian, C. Liu, I. Belopolski, T.-R. Chang, H.-T. Jeng, H. Lin *et al.*, Observation of a three-dimensional topological Dirac semimetal phase in high-mobility Cd_3As_2, Nat. Commun. **5**, 3786 (2014).

[49] W. Liu, X. Zhang, W. Meng, Y. Liu, X. Dai, and G. Liu, Theoretical realization of hybrid Weyl state and associated high catalytic performance for hydrogen evolution in NiSi, iScience **25**, 103543 (2022).

[50] W. Meng, X. Zhang, Y. Liu, X. Dai, and G. Liu, Antiferromagnetism caused by excess electrons and multiple topological electronic states in the electride $Ba_4Al_5 \cdot e^-$, Phys. Rev. B **104**, 195145 (2021).